

Materials Research Letters



ISSN: (Print) 2166-3831 (Online) Journal homepage: https://www.tandfonline.com/loi/tmrl20

Non-classical crystallographic slip in a ternary carbide – Ti₂AlC

Zhiqiang Zhan, Yexiao Chen, Miladin Radovic & Ankit Srivastava

To cite this article: Zhiqiang Zhan, Yexiao Chen, Miladin Radovic & Ankit Srivastava (2020) Non-classical crystallographic slip in a ternary carbide – Ti₂AlC, Materials Research Letters, 8:7, 275-281, DOI: 10.1080/21663831.2020.1748733

To link to this article: https://doi.org/10.1080/21663831.2020.1748733

Published online: 15 Apr 2020. Submit your article to this journal Article views: 397 View related articles View Crossmark data Citing articles: 1 View citing articles	9	© 2020 The Author(s). Published by Informa UK Limited, trading as Taylor & Francis Group
Article views: 397 View related articles View Crossmark data		Published online: 15 Apr 2020.
View related articles ☑ View Crossmark data ☑		Submit your article to this journal 🗗
View Crossmark data	ılıl	Article views: 397
CrossMark	Q [\]	View related articles 🗗
Citing articles: 1 View citing articles	CrossMark	View Crossmark data 🗷
	4	Citing articles: 1 View citing articles 🗗





ORIGINAL REPORT

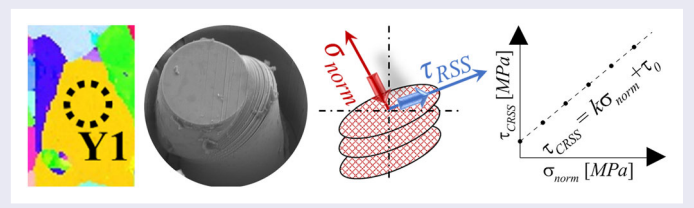


Non-classical crystallographic slip in a ternary carbide – Ti₂AlC

Zhigiang Zhan, Yexiao Chen, Miladin Radovic Dand Ankit Srivastava

Department of Materials Science and Engineering, Texas A&M University, College Station, TX, USA

Herein, we report on mechanical deformation of single-crystal Ti₂AlC MAX phase using compression testing of micropillars with a range of crystallographic orientations. Our results show that depending on the crystallographic orientation, the Ti₂AlC micropillars either undergo only non-classical (non-Schmid) crystallographic slip, non-classical crystallographic slip followed by cleavage or cleavage without any appreciable crystallographic slip. The non-classical crystallographic slip is found to be a result of the strong dependence of crystallographic slip on both, the resolved shear stress and the stress normal to the slip plane.



IMPACT STATEMENT

This work elucidates single-crystal level non-classical deformation mechanism(s) of a MAX phase and unravels the observed extreme plastic anisotropy of MAX phases.

ARTICLE HISTORY

Received 29 December 2019

KEYWORDS

MAX phase: micropillar compression; non-schmid slip; cleavage cracking; anisotropic deformation

Introduction

A family of ternary carbides and nitrides with the general formula $M_{n+1}AX_n$, where M is an early transitional metal, A is mostly from groups 13 to 16, X is carbon or nitrogen and *n* varies from 1 to 3, are referred to as MAX phases [1]. These are lightweight, stiff, thermodynamically stable and refractory, like ceramics, but damagetolerant, (pseudo) ductile at elevated temperatures and readily machinable, like metals [2,3]. Many of the unique properties of MAX phases are attributed to their nanolayered hexagonal crystal structure, where M elements are close-packed with X atoms in the octahedral sites and $M_{n+1}X_n$ layers are interleaved with A layers [3]. However, the nanolayered hexagonal crystal structure renders MAX phases extreme plastic anisotropy and they lack five independent slip systems needed to accommodate an arbitrary shape change [3,4].

While MAX phases have only two independent basal slip systems [5-7], the existence of additional deformation and failure mechanisms facilitated by their nanolayered structure distinguishes them from other materials with an insufficient number of slip systems. The weakly bonded MX-A interlayers in the MAX phases not only facilitate crystallographic slip but also cleavage, buckling of layers, ripplocations and kinking [3,4,8–12]. All these additional deformation and failure modes of MAX phases also contribute to their anisotropic mechanical behavior. Indeed, textured polycrystalline MAX phases in compression exhibit ductile response even at room temperatures with strain to failure exceeding 10% [13]. Thus, it is important to understand the single-crystal level mechanical response of MAX phases to unravel the observed extreme plastic anisotropy of polycrystalline MAX phases at macroscale.

Several attempts have been made to characterize the single-crystal level mechanical response of MAX phases using nanoindentation [9-11,14,15]. However, the indentation experiments by nature are extremely non-linear and the stress-strain state during indentation are quite complex. A more direct approach to characterize the single-crystal level mechanical response of a polycrystalline material is using micropillar compression tests [16]. In this approach, micropillar specimens are milled from individual grains and are subsequently deformed under uniaxial compression with a flat-punch nanoindenter. Recently, limited micropillar compression tests of Ti₂InC [17], Ti₄AlN₃ [17] and Ti₃SiC₂ [18] MAX phases have been carried out. These tests have shown that under circumstances where crystallographic slip is not restricted, basal slip is the only operative deformation mechanism in MAX phases. Building on these recent works, here we carry out an exhaustive micropillar compression tests of Ti₂AlC MAX phase with a wide range of crystallographic orientations.

Out of most MAX phases, Ti₂AlC is one of the most promising materials for structural applications in air and humid environments at high temperature, due to its high oxidation resistance provided by self-forming Al₂O₃ protective layer [19]. Our micropillar compression test results show that depending on the crystallographic orientation, Ti₂AlC MAX phase either undergoes only non-classical crystallographic slip, non-classical crystallographic slip followed by cleavage or cleavage without any appreciable crystallographic slip. We note that nonclassical crystallographic slip, i.e. violation of Schmid's law has been readily observed in bcc metals [20–24], but to the best of our knowledge, this is the first observation of non-classical crystallographic slip in a MAX phase.

Material and method

A two-step process was followed to produce high-purity Ti₂AlC MAX phase. In this process, Ti₂AlC powder was first synthesized by pressure less sintering and then densified into bulk compact material by Spark Plasma Sintering, for more details, see ref. [25]. The fully dense Ti₂AlC sample was annealed at 1400°C in a high-vacuum tube furnace under Ar atmosphere for 48 h to obtain coarsegrained microstructure. The coarse-grained Ti₂AlC sample was mechanically polished using diamond paste and colloidal silica suspension, following procedure detailed in ref. [26]. The electron backscatter diffraction orientation maps were acquired from the polished samples using a Tescan FERA-3 model GMH focused ion beam (FIB) microscope with a spatial resolution of $\sim 1.5 \,\mu \text{m}$. Subsequently, cylindrical micropillar compression specimens were milled from grains of known crystallographic orientations using a Tescan Lyra-3 model GMH FIB Microscope with 30 keV Ga ions. The top diameters of the micropillars were $\sim 10 \, \mu \text{m}$ with a vertical taper of \sim 4° and height/diameter ratio were \sim 2. The micropillars were deformed under uniaxial compression in ambient conditions using a Hysitron TI 950 triboindenter

equipped with a 20 μ m diameter flat-punch diamond tip at a loading rate of 0.3 mN/s. The load-displacement data obtained from the nanoindenter were converted to nominal (engineering) stress and strain, where the nominal stress was calculated by averaging the diameters at the top and the mid-section of the micropillars. The secondary electron images of all the deformed micropillars were also acquired using the scanning electron microscope in Tescan FERA-3.

Results and discussion

The microstructure of annealed Ti₂AlC MAX phase contains elongated grains with an average grain length of \sim 100 μ m, Figure 1(a). Several micropillars were milled from large grains with different crystallographic orientations. Selected but typical SEM image of an as-milled micropillar is shown in Figure 1(c). The grains from which micropillars were milled are indicated in the EBSD maps in Figure 1(a) and their crystallographic orientation in terms of Euler angles $(\varphi_1, \phi, \varphi_2)$ are given in Table 1. The MAX phases are *hcp* crystals with two independent basal slip systems, (0001) < 1120 >, as the dominant slip systems. Following this, the maximum Schmid factor, $\mu_{\max}^{\alpha} = \max(\mu^{\alpha})$, (where μ^{α} is the Schmid factor for αth basal slip system) for all micropillars are also given in Table 1.

To calculate the Schmid factor, μ^{α} , for α th basal slip system, the slip plane normal, m, and the three slip directions, s^{α} , are first transformed from the four-index scheme, (hkil)[uvtw], to a three-axis orthogonal coordinate system, (h'k'l')[u'v'w'], using the relation,

$$m_{i} = (h', k', l') = \left(2h + k, \sqrt{3}k, \sqrt{3}l\frac{a}{c}\right);$$

$$s_{i}^{\alpha} = [u', v', w'] = \left[(2u + v)\frac{\sqrt{3}}{2}, v\frac{3}{2}, w\frac{c}{a}\right]$$
(1)

The slip system written in the three-axis orthogonal coordinate system are then normalized and rotated into the fixed (sample) frame of the micropillars as, $\tilde{m}_i =$ $g_{ii}(m_i/|m_i|)$ and $\tilde{s}_i^{\alpha} = g_{ii}(s_i^{\alpha}/|s_i^{\alpha}|)$, where the rotation tensor, g_{ij} , in terms of the Euler angles are given by,

$$g_{ij} = \begin{cases} \cos \varphi_1 \cos \varphi_2 - \sin \varphi_1 \cos \phi \sin \varphi_2 \\ \sin \varphi_1 \cos \varphi_2 + \cos \varphi_1 \cos \phi \sin \varphi_2 \\ \sin \varphi_2 \sin \phi \end{cases}$$

$$-\cos \varphi_1 \sin \varphi_2 - \sin \varphi_1 \cos \phi \cos \varphi_2 \quad \sin \varphi_1 \sin \phi \\ -\sin \varphi_1 \sin \varphi_2 + \cos \varphi_1 \cos \phi \cos \varphi_2 \quad -\cos \varphi_1 \sin \phi \\ \cos \varphi_2 \sin \phi \quad \cos \phi \end{cases}$$
(2)

Now, given the (compression) axis of the micropillar is along z, [001], in the fixed sample frame, the Schmid factor for α th slip system is calculated as, $\mu^{\alpha} = (z_i \tilde{m}_i)(z_i \tilde{s}_i^{\alpha})$.

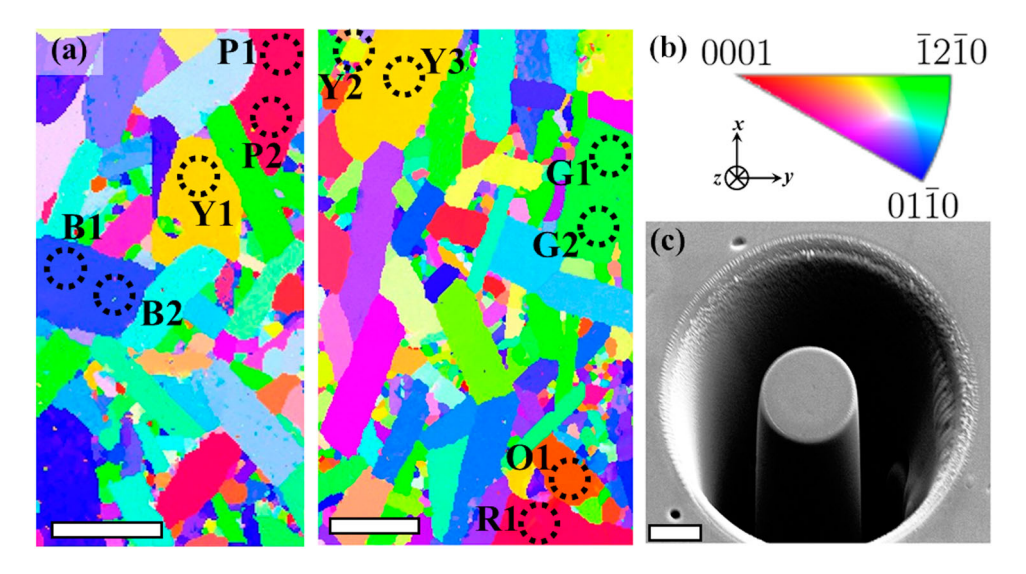


Figure 1. (a) EBSD maps of the microstructure of Ti₂AIC MAX phase indicating grains (dotted circles) from which micropillars were subsequently milled. (b) The color-coded stereographic triangle associated with the z-axis EBSD maps in (a). (c) Selected but typical SE-SEM image of an as milled micropillar with axis along z. The scale bar in (a) is 100 μ m and in (c) is 5 μ m.

Table 1. Euler angles and maximum Schmid factor, μ_{\max}^{α} , for all the micropillars.

		Euler angles		
Micropillar	Max. Schmid factor	$arphi_1$	ϕ	$arphi_2$
B1, B2	0.15 ± 0.01	168° ± 0.3	80° ± 0.3	37° ± 0.2
Y1	0.50 ± 0.001	$85^{\circ} \pm 0.3$	$139^{\circ} \pm 0.2$	$59^{\circ} \pm 0.2$
Y2	0.50 ± 0.001	$163^{\circ} \pm 0.3$	$47^{\circ} \pm 0.3$	$60^{\circ} \pm 0.2$
Y3	0.50 ± 0.0001	$65^{\circ} \pm 0.2$	$44^{\circ}\pm0.2$	$56^{\circ} \pm 0.2$
P1, P2	0.35 ± 0.003	$68^{\circ} \pm 0.6$	$155^{\circ} \pm 0.3$	$35^{\circ} \pm 0.5$
G1, G2	0.07 ± 0.01	$75^{\circ} \pm 0.3$	$86^{\circ} \pm 0.5$	$7^{\circ} \pm 0.3$
01	0.31 ± 0.003	$137^{\circ} \pm 0.4$	$161^{\circ} \pm 0.2$	$1^{\circ}\pm0.4$
R1	$\textbf{0.30} \pm \textbf{0.01}$	$161^{\circ} \pm 1.1$	$159^{\circ}\pm1.0$	$32^{\circ} \pm 1.0$

The maximum Schmid factor, μ_{\max}^{α} , of the micropillars considered in this work varies over a wide range, i.e. from 0.07 to 0.5, see Table 1.

The nominal compression stress–strain curves for O1, Y1 and Y3 micropillars are shown in Figure 2(a). The Y1 and O1 micropillars were deformed to large compressive strains, whereas the compressive deformation of Y3 micropillar was interrupted after achieving $\sim 3\%$ strain. The stress-strain response of all three micropillars exhibit three characteristic stages. In the initial stage the stress-strain response appears to be linear and with continued deformation the stress-strain response deviates from linearity marking the onset of yielding. Following yielding, a brief period of steep strain-hardening is observed, and with further increase in deformation, the strain-hardening rate decreases appreciably. Also, the extent of steep strain-hardening post yielding in the micropillars depends on the crystallographic orientation. All three micropillars O1, Y1 and Y3 are oriented for a single slip with the values of μ_{\max}^{α} being 0.31, 0.50 and 0.50, respectively, on one of the three α th

basal slip systems. The post-deformation observation of all three micropillars in the SEM indeed shows deformation by crystallographic slip on a single slip system, Figure 2(b,d,e). The deformation by crystallographic slip is confirmed by the SEM image of deformed Y1 micropillar after ion-polishing in Figure 2(c) that does not show any remnant features. The post-deformation SEM image of O1 micropillar, however, differs from that of Y1 and Y3 micropillars. As shown in Figure 2(e), the O1 micropillar deformed like a slightly inclined stack of poker chips in contrast to Y1 and Y3 micropillars that underwent rather localized slip-on parallel slip planes.

The nominal compression stress-strain curves of micropillars with two lowest values of μ_{\max}^{α} are shown in Figure 3(a). The value of $\mu_{\rm max}^{\alpha}$ for micropillar B2 is 0.15 and that for micropillars G1 and G2 is 0.07. The stress–strain response of the B2 micropillar exhibits all three characteristic stages as was observed for the micropillars in Figure 2. However, the stress-strain response of G1 micropillar is almost linear all the way up to ~ 1.0 GPa and thereafter the load bearing capacity of the micropillar drops rapidly. The G2 micropillar that was milled from the same grain as the G1 micropillar and was deformed only up to $\sim 1\%$ compressive strain (or ~ 0.85 GPa stress level) confirmed the lack of early stage yielding in these micropillars. The postdeformation observation of B2 micropillar in the SEM, Figure 3(b,c), shows an onset of crystallographic slip on a single slip system which is followed by bulging and cleavage normal to the basal plane. The SEM image of deformed G2 micropillar, Figure 3(d), shows no remnant features of deformation and that of G1 micropillar, Figure 3(e), shows cleavage normal to the basal plane.

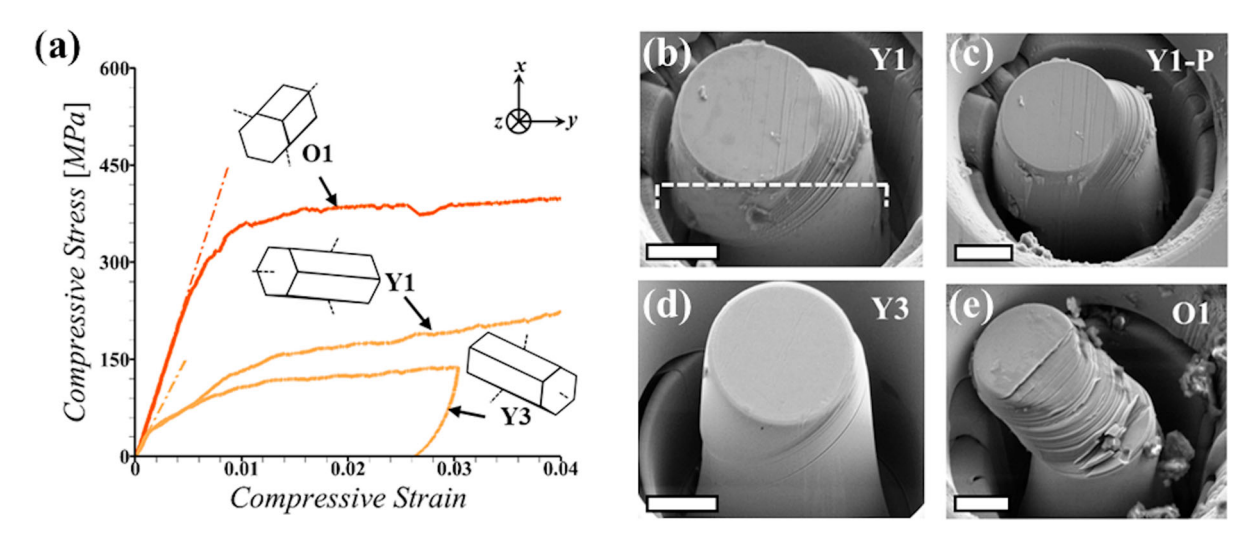


Figure 2. (a) Nominal compression stress–strain curves for micropillars milled from O1, Y1 and Y3 grains. The crystal orientations of all grains are shown as inset in (a). The dash-dot lines in (a) highlight the initial linear response of the micropillars. (b) SE-SEM image of the deformed micropillar milled from Y1 grain. (c) SE-SEM image of deformed micropillar in (b) that has been ion-polished along the dashed line shown in (b). SE-SEM images of deformed micropillars milled from (d) Y3 and (e) O1 grains. The scale bar in SEM images (b)–(e) is 5 μm.

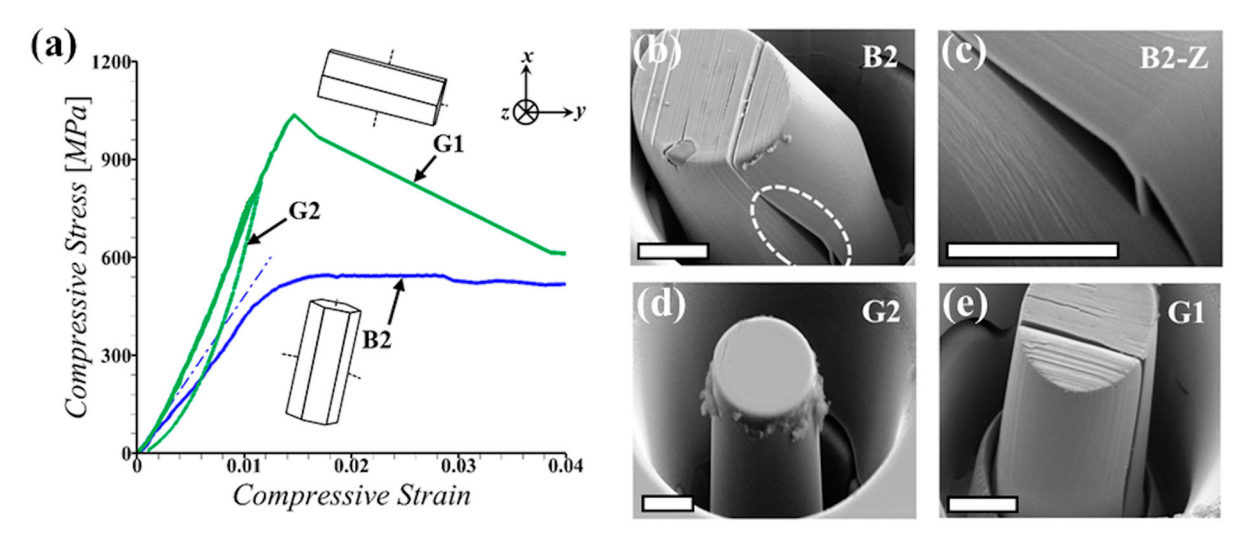


Figure 3. (a) Nominal compression stress–strain curves for micropillars milled from G1, G2 and B2 grains. The crystal orientations of all grains are shown as inset in (a). The dash-dot line in (a) highlights the initial linear response of B2 micropillar. (b) SE-SEM image of the deformed micropillar milled from B2 grain. (c) Zoomed view of the region marked by a dashed ellipse in (b). SE-SEM images of deformed micropillars milled from (d) G2 and (e) G1 grains. The scale bar in SEM images (b)–(e) is 5μm.

The results presented in Figures 2 and 3 clearly show that at single-crystal level the mechanical response of Ti₂AlC MAX phase is extremely anisotropic. This is further highlighted in Figure 4(a) where the nominal compression stress–strain curves of six micropillars with the values of $\mu_{\rm max}^{\alpha}$ ranging from 0.07 to 0.5 are compared. To an extent, the extremely anisotropic mechanical response of micropillars is because, depending on the crystallographic orientation, the micropillars either undergo only crystallographic slip, crystallographic slip followed by cleavage or cleavage without appreciable crystallographic slip. The activation of cleavage in the

micropillars of Ti₂AlC MAX phase with low values of $\mu_{\rm max}^{\alpha}$ is in contrast to the observed deformation of micropillars of *hcp* metals with similar values of $\mu_{\rm max}^{\alpha}$. For example, the micropillars of titanium with low values of $\mu_{\rm max}^{\alpha}$ undergoes deformation by prismatic slip [27] while under similar circumstances twinning is observed in magnesium [28].

All the micropillars except G1–G2 micropillars exhibit initial yielding, Figure 4(a). The stress at the initial yield point, σ_0 , of these micropillars is identified as the point of intersection between the stress–strain curve and a straight line with a slope equal to 95% of the average slope

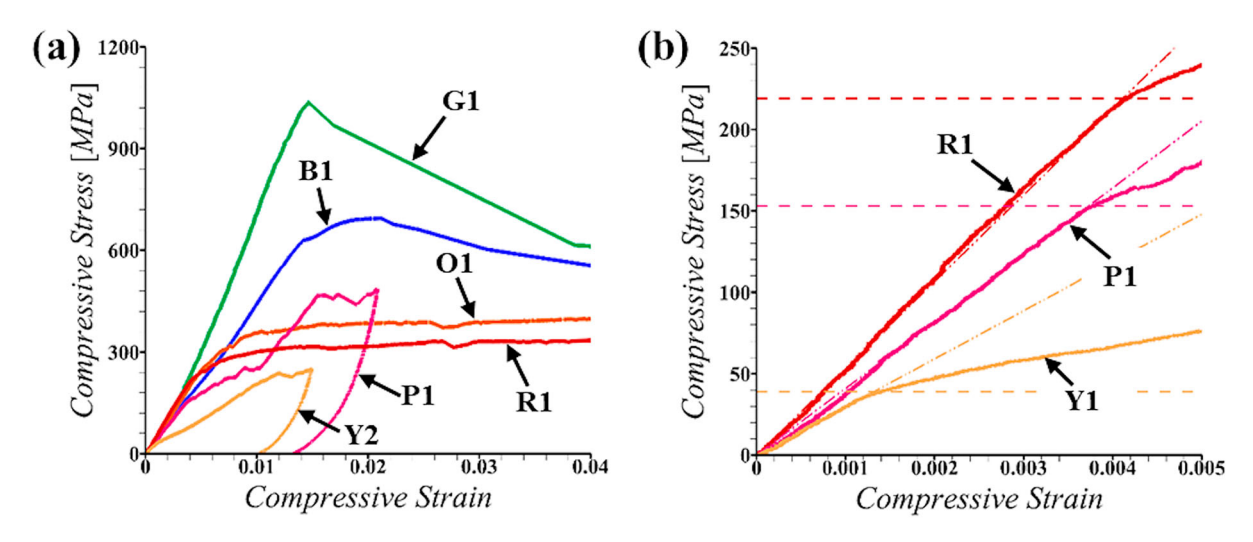


Figure 4. (a) Nominal compression stress–strain curves for micropillars milled from six grains. (b) Early stage compression stress–strain curves showing the onset of yielding in the stress–strain response of micropillars milled from three grains.

of the initial linear portion of the stress–strain curve, Figure 4(b). For micropillar R1, $\sigma_0 \approx 219$ MPa and for micropillar Y1, $\sigma_0 \approx 39$ MPa. This results in the value of critical resolved shear stress, $\tau_{CRSS} = \sigma_0 \times \mu_{max}^{\alpha}$, to be ~ 65.7 MPa for R1 and ~ 19.5 MPa for Y1 micropillar. Thus, the value of τ_{CRSS} for Ti₂AlC MAX phase depends on the crystallographic orientation which is contrary to the classical Schmid's law. The classical Schmid's law predicts that the value of τ_{CRSS} is a material property and is independent of the crystallographic orientation.

We hypothesize that the non-classical crystallographic slip in Ti₂AlC MAX phase is most likely due to the fact that crystallographic slip in this material not only depends on the resolved shear stress, $\tau_{\rm RSS} = \sigma \cos \psi \cos \lambda$, but also on the stress normal to the slip (basal) plane, $\sigma_{\rm norm} = \sigma(\cos \psi)^2$, as shown schematically in Figure 5(a) where $\cos \psi = z_i \tilde{m}_i$, $\cos \lambda = \max(z_i \tilde{s}_i^{\alpha})$, and σ is the imposed compressive stress. To test this hypothesis, the variation of $\tau_{\rm CRSS}$ with $\sigma_{\rm norm}$ is plotted in Figure 5(b) for nine micropillars. As shown in Figure 5(b), the variation of $\tau_{\rm CRSS}$ with $\sigma_{\rm norm}$ can be represented as, $\tau_{\rm CRSS} = k\sigma_{\rm norm} + \tau_0$, where k = 0.28 and $\tau_0 = 13.8$ MPa are the fitting constants.

Non-classical crystallographic slip, i.e. violation of Schmid's law has been readily observed in *bcc* metals [20–24], and it has been postulated that it is due to the non-planar spreading of the screw dislocation core in the presence of stresses other than the resolved shear stress [23]. In MAX phases, dislocation glide is confined to the basal plane [5–7], and in ref. [6], it was shown that this results in strong interactions and dislocation alignments along specific orientations that may lead to elevated lattice friction. The latter can give rise to non-classical crystallographic slip shown in Figure 5(b). However, the

strength of some other layered materials such as Mica also exhibits (confining) pressure sensitivity [29]. More recently, it has been suggested that in layered materials, including MAX phases, ripplocations and not the basal dislocations are the operative micromechanism of deformation [12]. In principle, the value of τ_{CRSS} needed to move ripplocations will increase with an increase in stress normal to the basal plane [11], which can also give rise to non-classical crystallographic slip shown in Figure 5(b). Thus, more work is needed to confirm the micromechanism of non-classical crystallographic slip in MAX phases.

Next, we analyze the propensity of cleavage normal to the basal plane in a micropillar subjected to uniaxial compression. To this end, we compute the elastic strains in the micropillars using, $\varepsilon_{ij}^e = \tilde{S}_{ijkl}\sigma_{kl}$, where \tilde{S}_{ijkl} is the 4th rank compliance tensor and σ_{kl} is the imposed stress state, i.e. σ_{33} equals to unit compressive stress and all other components being zero. The compliance tensor, S_{iikl} , in the crystallographic orientation of the micropillar is obtained using the rotation tensor g_{ij} , Equation (2), and the values of the elastic constants of Ti₂AlC MAX phase calculated in ref. [30]. The elastic strain normal to the basal plane, $\varepsilon_{\text{norm}}$, in a micropillar is then obtained as, $\varepsilon_{\text{norm}} = \tilde{m}_i \varepsilon_{ii}^e \tilde{m}_j$. Out of all the micropillars considered here, the value of $\varepsilon_{\rm norm} > 0$ (tensile) only for B1–B2 and G1-G2 micropillars, with the value of $\varepsilon_{\text{norm}}$ for G1-G2 micropillars being greater than that for B1-B2 micropillars. This together with the fact that the value of μ_{\max}^{α} and hence τ_{RSS} for G1-G2 micropillars is very small, results in cleavage normal to basal plane without any appreciable crystallographic slip in these micropillars. While for B1–B2 micropillars, the value of μ_{\max}^{α} is reasonable, but the steep strain-hardening following initial

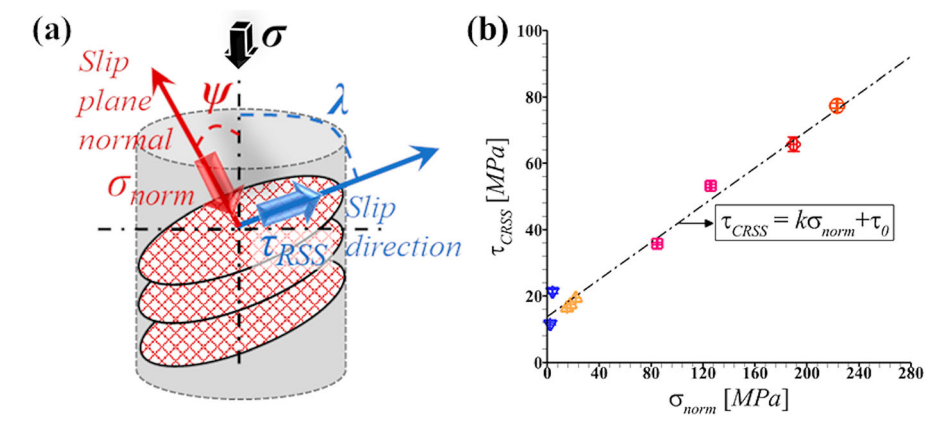


Figure 5. (a) A schematic showing the applied axial compressive stress, σ , on a cylindrical pillar, resolved normal stress, σ_{norm} , on the slip plane and resolved shear stress, τ_{RSS} , on the slip plane in the slip direction. (b) The variation of critical resolved shear stress, τ_{CRSS} (i.e. the value of $\tau_{\rm RSS}$ corresponding to the onset of yielding in the stress–strain response of micropillars), with $\sigma_{\rm norm}$

yielding makes continual crystallographic slip harder. Thus, resulting in cleavage normal to the basal plane post limited crystallographic slip.

Conclusion

The single-crystal level mechanical response and deformation mechanism of Ti₂AlC MAX phase have been elucidated using compression tests of micropillars with a range of crystallographic orientations. The results show that depending on the crystallographic orientation, the material can either undergo only non-classical (non-Schmid) crystallographic slip, non-classical crystallographic slip followed by cleavage or cleavage without appreciable crystallographic slip. The non-classical crystallographic slip is revealed to be a result of the strong dependence of crystallographic slip on both, the resolved shear stress and the stress normal to the slip plane. While the onset of cleavage normal to the basal plane is found to be associated with the difficulty of crystallographic slip and tensile strain normal to the basal plane. The microscale single-crystal level deformation mechanism elucidated here will potentially help unravel the observed extreme plastic anisotropy of polycrystalline MAX phases at the macroscale.

Disclosure statement

No potential conflict of interest was reported by the author(s).

Funding

This work was supported by the U.S. National Science Foundation award number CMMI-1729350.

ORCID

Miladin Radovic http://orcid.org/0000-0003-4571-2848

References

- [1] Barsoum MW, El-Raghy T. The MAX phases: unique new carbide and nitride materials ternary ceramics turn out to be surprisingly soft and machinable, yet also heat-tolerant, strong and lightweight. Am Scientist. 2001;89(4):334-343.
- [2] Radovic M, Barsoum MW. MAX phases: Bridging the gap between metals and ceramics [Article]. Am Ceram Soc Bull. 2013;92(3):20-27.
- [3] Barsoum MW, Radovic M. Elastic and mechanical properties of the MAX phases. Annu Rev Mater Res. 2011;41(1):195-227.
- [4] Farber L, Barsoum MW, Zavaliangos A, et al. Dislocations and Stacking Faults in Ti3SiC2. J Am Ceram Soc. 1998;81(6):1677-1681.
- [5] Barsoum MW, Farber L, Levin I, et al. High-resolution transmission electron microscopy of Ti4AlN3, or Ti3A 12N2 revisited. J Am Ceram Soc. 1999;82(9):2545-2547.
- [6] Guitton A, Joulain A, Thilly L, et al. Dislocation analysis of Ti2AlN deformed at room temperature under confining pressure. Philos Mag. 2012;92(36):4536-4546.
- [7] Gouriet K, Carrez P, Cordier P, et al. Dislocation modelling in Ti2AlN MAX phase based on the Peierls-Nab arro model. Philos Mag. 2015;95(23):2539-2552.
- [8] Barsoum MW, Farber L, El-Raghy T. Dislocations, kink bands, and room-temperature plasticity of Ti3SiC2 [journal article]. Mat Trans A. 1999;30(7):1727-1738.
- [9] Molina-Aldareguia JM, Emmerlich J, Palmquist J-P, et al. Kink formation around indents in laminated Ti3SiC2 thin films studied in the nanoscale. Scr Mater. 2003;49(2):155-160.
- [10] Kooi BJ, Poppen RJ, Carvalho NJM, et al. Ti3SiC2: A damage tolerant ceramic studied with nano-indentations and transmission electron microscopy. Acta Mater. 2003;51 (10):2859-2872.
- [11] Griggs J, Lang AC, Gruber J, et al. Spherical nanoindentation, modeling and transmission electron microscopy evidence for ripplocations in Ti3SiC2. Acta Mater. 2017;131:141-155.
- [12] Barsoum M, Tucker G. Deformation of layered solids: ripplocations not basal dislocations. Scr Mater. 2017;139: 166-172.



- [13] Barsoum MW, El-Raghy T. Room-temperature, ductile carbides [Article]. Metall Mat Trans A. 1999;30(2):363-
- [14] Barsoum MW, Murugaiah A, Kalidindi SR, et al. Kink bands, nonlinear elasticity and nanoindentations in graphite. Carbon N Y. 2004;42(8):1435-1445.
- [15] Tromas C, Villechaise P, Gauthier-Brunet V, et al. Slip line analysis around nanoindentation imprints in Ti3SnC2: a new insight into plasticity of MAX-phase materials. Philos Mag. 2011;91(7-9):1265-1275.
- [16] Uchic MD, Dimiduk DM, Florando JN, et al. Sample dimensions influence strength and crystal plasticity. Science. 2004;305(5686):986-989.
- [17] Brüsewitz C, Knorr I, Hofsäss H, et al. Single crystal pillar microcompression tests of the MAX phases Ti2InC and Ti4AlN3. Scr Mater. 2013;69(4):303-306.
- [18] Higashi M, Momono S, Kishida K, et al. Anisotropic plastic deformation of single crystals of the MAX phase compound Ti3SiC2 investigated by micropillar compression. Acta Mater. 2018;161:161-170.
- [19] Sundberg M, Malmqvist G, Magnusson A, et al. Alumina forming high temperature silicides and carbides. Ceram Int. 2004;30(7):1899-1904.
- [20] Christian J. Some surprising features of the plastic deformation of body-centered cubic metals and alloys. Metall Trans A. 1983;14(7):1237-1256.
- [21] Taylor G. Thermally-activated deformation of BCC metals and alloys. Prog Mater Sci. 1992;36:29-61.
- [22] Qin Q, Bassani JL. Non-schmid yield behavior in single crystals. J Mech Phys Solids. 1992;40(4):813-833.

- [23] Duesbery M-S, Vitek V. Plastic anisotropy in bcc transition metals. Acta Mater. 1998;46(5):1481-1492.
- [24] Srivastava A, Ghassemi-Armaki H, Sung H, et al. Micromechanics of plastic deformation and phase transformation in a three-phase TRIP-assisted advanced high strength steel: experiments and modeling. J Mech Phys Solids. 2015;78:46-69.
- [25] Benitez R, Kan WH, Gao H, et al. Room temperature stress-strain hysteresis in Ti2AlC revisited. Acta Mater. 2016;105:294-305.
- [26] Benitez R, Kan WH, Gao H, et al. Mechanical properties and microstructure evolution of Ti2AlC under compression in 25-1100°C temperature range. Acta Mater. 2020;189:154-165.
- [27] Sun Q, Guo Q, Yao X, et al. Size effects in strength and plasticity of single-crystalline titanium micropillars with prismatic slip orientation. Scr Mater. 2011;65(6): 473-476.
- [28] Liu Y, Li N, Arul Kumar M, et al. Experimentally quantifying critical stresses associated with basal slip and twinning in magnesium using micropillars. Acta Mater. 2017;135:411-421.
- [29] Shea WT, Kronenberg AK. Rheology and deformation mechanisms of an isotropic mica schist. J Geophys Res Solid Earth. 1992;97(B11):15201-15237.
- [30] Du Y, Sun Z, Hashimoto H, et al. Theoretical investigations on the elastic and thermodynamic properties of Ti2AlC0.5N0.5 solid solution. Phys Lett A. 2009;374(1):78-82.